INTERNATIONAL JOURNAL FOR NUMERICAL METHODS IN FLUIDS
Int. J. Numer. Meth. Fluids 2000; **33**: 59–79

A Legendre-spectral element method for flow and heat transfer about an accelerating droplet

Seyoung Oh[a], Hoa D. Nguyen[b] and Seungho Paik[c,*,1]

[a] *Department of Mathematics, Chungnam National University, Taejon, South Korea*
[b] *Innovative Engineering Solutions, Idaho Falls, ID, U.S.A.*
[c] *Idaho National Engineering Environmental Laboratory, Idaho Falls, ID, U.S.A.*

SUMMARY

The problem of flow and heat transfer associated with a spherical droplet accelerated from rest under gravitational force is studied using a Legendre-spectral element method in conjunction with a mixed time integration procedure to advance the solution in time. An influence matrix technique that exploits the superposition principle is adapted to resolve the lack of vorticity boundary conditions and to decouple the equations from the interfacial couplings. The computed flow and temperature fields, the drag coefficient, the Nusselt number, and the interfacial velocity and vorticity are presented for a drop moving vertically in a quiescent gas of infinite extent to illustrate the evolution of the flow and temperature fields. Comparison of the predicted drag coefficient and the Nusselt number against previous numerical and experimental results indicate good agreement. Copyright © 2000 John Wiley & Sons, Ltd.

KEY WORDS: droplet; Legendre-spectral element method; vorticity

1. INTRODUCTION

Droplet transport processes are of fundamental importance in many applications ranging from natural phenomena to industrial processes, including space operations. Typical examples are the transport associated with rain drops, the heat/mass transfer in dispersive extraction processes, the energy removal systems in space, such as the liquid droplet radiator, to name a few. As indicated in the literature, it has long been a subject of great interest and can be traced back to the pioneering works of Hadamard [1] and Rybczynski [2], who independently derived the analytical solution for creeping flow around a fluid sphere. Although their theory is strictly developed for zero Reynolds number, it has provided a mathematical foundation for subsequent works to aim at improving the solution as the inertial terms are accounted for.

* Correspondence to: Idaho National Engineering Environmental Laboratory, Idaho Falls, ID, 83415-3880, U.S.A.
[1] Tel.: + 1 208 5266866.

Received 7 June 1997
Revised 27 June 1999

Two notable types of solutions have emerged including the boundary layer solutions [3] and the perturbation solutions [4], which are valid for high- and low-Reynolds number regimes respectively. Despite these solutions being analytical, the applicability of these solutions is rather limited because it is the intermediate Reynolds number range that one encounters in most practical situations. More recently, the advances of computer technologies, both in hardware and software, have created a new opportunity for solving problems that were otherwise intractable. Consequently, numerical results for the full Navier–Stokes equations at intermediate Reynolds numbers are being reported at a faster pace than ever before. Representative examples include finite difference solutions [5], partial spectral solutions [6,7], a full spectral solution [8], etc. Heat transfer in this Reynolds number range has been considered by Oliver and Chune [9,10] under quasi-steady conditions and by Nguyen *et al.* [11] under full transient conditions.

As has been proven in the monograph of Gottlieb and Orszag [12], global expansions would give the result that has an infinite order of accuracy. However, such a desirable feature disappears when used in combination with either finite differences [6] or finite elements [7] because the overall accuracy of the numerical scheme is dictated by the lower-order method. Motivated by the loss of accuracy, we proposed [8] a full spectral method in that the dependent variables are expanded as a double series of Legendre and Chebyshev polynomials in the angular and radial directions respectively. Unfortunately, their method is computationally inefficient because inverting a spectral matrix is much more expensive than those resulting from finite differences and finite elements.

The purpose of this work is to develop a strategy that is spectrally accurate while preserving the banded structure of the matrices so as to increase the computational efficiency of full spectral schemes. The innovation of the present study is twofold. First, a Legendre-spectral element is developed with a spectral element [13] used in place of the Chebyshev collocation as employed by us [8]. It is expected that this modification would lead to a reduction of the computational cost and will offer a greater flexibility for grid refinement, but at a price of a small loss in accuracy, which is typically unimportant in the practical sense. Second, the present numerical model features the use of the influence matrix technique to resolve the absence of vorticity boundary conditions as well as to decouple the equations from phase couplings at the drop surface. Numerical tests are performed on the dynamics and heat transfer of droplet falling under gravity in another fluid having a temperature different from the droplet temperature. This type of problem is characterized by a time-dependent particle velocity, dictated by a trajectory equation that must be solved along with the flow equations, and has been examined to some extent by Lin and Lee [14] for a solid sphere and by Chisnell [15] for a liquid drop falling at low Reynolds numbers.

2. GOVERNING EQUATIONS

Predicting the hydrodynamics and heat transfer associated with a droplet requires the solution of the mass continuity, momentum and energy equations. Provided no droplet deformation occurs and the fluid is incompressible and Newtonian with constant physical properties, these equations can be written in dimensionless form as

$$E^2\psi = -r\omega \sin\theta \tag{1}$$

$$\frac{\partial\omega}{\partial t} - \frac{Re}{2r}\frac{\partial(\psi, \omega/r\sin\theta)}{\partial(r,\theta)} = \frac{\Phi_v}{r\sin\theta}E^2(\omega r\sin\theta) - \frac{\omega}{Re}\frac{\mathrm{d}Re}{\mathrm{d}t} \tag{2}$$

$$Pr\frac{\partial\zeta}{\partial t} - \frac{Pe}{2r^2\sin\theta}\frac{\partial(\psi,\zeta)}{\partial(r,\theta)} = \Phi_\alpha\nabla^2\zeta \tag{3}$$

in which the last term on the right-hand side of Equation (2) was introduced through non-dimensionalization. In this process, the radius r has been made dimensionless with R, the time t with R^2/v, the streamfunction ψ with R^2U_p, and the vorticity ω with U_p/R. Here R is the droplet radius, U_p is the (unknown) droplet translational velocity, v is the kinematic viscosity of the fluid, and θ is the angular co-ordinate as shown in Figure 1. The dimensionless groups appearing in the above equations are the Peclet number (Pe), the Prandtl number (Pr) and the Reynolds number (Re), and were defined based on the droplet diameter, droplet velocity and the properties of the continuous phase. Φ_v and Φ_α are the kinematic viscosity and the thermal diffusivity ratios respectively of the interior to the exterior fluids. For convenience, we have used $\partial(\ ,\ )/\partial(\ ,\ )$ to denote the Jacobian and the operators E^2 and ∇^2 are defined as

$$E^2 \equiv \frac{\partial^2}{\partial r^2} + \frac{\sin\theta}{r^2}\frac{\partial}{\partial\theta}\left(\frac{1}{\sin\theta}\frac{\partial}{\partial\theta}\right) \tag{4a}$$

$$\nabla^2 \equiv \frac{1}{r^2}\frac{\partial}{\partial r}\left(r^2\frac{\partial}{\partial r}\right) + \frac{1}{r^2\sin\theta}\frac{\partial}{\partial\theta}\left(\sin\theta\frac{\partial}{\partial\theta}\right) \tag{4b}$$

Since the streamfunction is defined such that the continuity equation is satisfied exactly, the velocity vector $\mathbf{u}$ can be expressed in terms of the streamfunction as

$$\mathbf{u} = \frac{\mathbf{e}_r}{r^2\sin\theta}\frac{\partial\psi}{\partial\theta} - \frac{\mathbf{e}_\theta}{r\sin\theta}\frac{\partial\psi}{\partial r} \tag{5}$$

where $\mathbf{e}_r$ and $\mathbf{e}_\theta$ are the unit vectors in the radial and angular directions respectively.

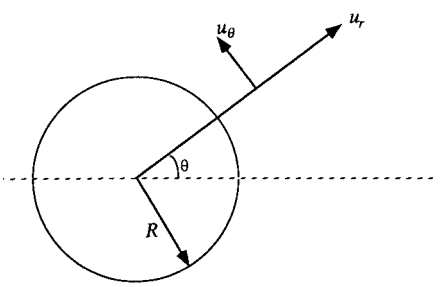

Figure 1. Co-ordinates of the physical system.

Unlike the case of a droplet moving at its terminal velocity or a droplet experiencing a constant uniform velocity, an accelerating droplet is characterized by a time-dependent velocity that must be calculated from the trajectory equation. When the gravity and the drag force, assuming negligible Basset history as justified by $\Phi_\rho \gg 1$, are taken into account this equation becomes [14]

$$\frac{\mathrm{d}(Re)}{\mathrm{d}t} + \frac{3C_\mathrm{D}}{16\Phi_\rho} Re^2 = \frac{2gR^3}{\nu^2}\left(1 - \frac{1}{\Phi_\rho}\right) \tag{6}$$

where C_D is the drag coefficient and is a function of the Reynolds number and the viscosity ratio, g is the acceleration of the gravity, ν is the kinematic viscosity of the external fluid, and Φ_ρ is the density ratio of the dispersed phase to that of the continuous phase.

It is worthwhile at this point to add two remarks: First, Equations (1)–(5) hold for both fluid inside and outside the droplet as long as the values of Φ_α and Φ_ν are assigned according to the convention that Φ_α and Φ_ν are unity for the continuous phase and the appropriate ratio for the droplet phase. To avoid confusion, a tilde ($\sim$) is used to distinguish the droplet phase hereafter. Second, the term on the right-hand side of Equation (6) can be interpreted as the initial acceleration of the drop; hence we shall abbreviate it by Γ.

In order to obtain a particular solution, the above system of equations is solved subjected to the following conditions:

A. *Along the line of symmetry*

$$\psi(t, r, 0) = \psi(t, r, \pi) = \tilde{\psi}(t, r, 0) = \tilde{\psi}(t, r, \pi) = 0 \tag{7a}$$

$$\omega(t, r, 0) = \omega(t, r, \pi) = \tilde{\omega}(t, r, 0) = \tilde{\omega}(t, r, \pi) = 0 \tag{7b}$$

$$\zeta(t, r, 0) = \zeta(t, r, \pi) = \tilde{\zeta}(t, r, 0) = \tilde{\zeta}(t, r, \pi) = 0 \tag{7c}$$

B. *At the free stream*

$$\lim_{r\to\infty} \psi(t, r, \theta) \to \frac{r^2}{2}\sin^2\theta, \qquad \lim_{r\to\infty} \omega(t, r, \theta) \to 0, \qquad \lim_{r\to\infty} \zeta \to 0 \tag{8a,b,c}$$

where the limit $r \to \infty$ is computationally interpreted as a fixed radius, r_∞, which is the radius beyond which the flow is considered uniform.

C. *Along the interface*

$$\frac{\partial\psi}{\partial r} = \frac{\partial\tilde{\psi}}{\partial r}, \qquad \frac{\partial\psi}{\partial\theta} = 0, \qquad \frac{\partial\tilde{\psi}}{\partial\theta} = 0, \qquad \omega - 2u_\theta = \Phi_\mu(\tilde{\omega} - 2\tilde{u}_\theta) \tag{9a,b,c,d}$$

$$\zeta = \tilde{\zeta}, \qquad \frac{\partial \zeta}{\partial r} = \Phi_\kappa \frac{\partial \tilde{\zeta}}{\partial r} \tag{9e,f}$$

D. *At the drop center*

$$\tilde{\psi} \to 0, \qquad \tilde{\omega} \to 0, \qquad \tilde{\zeta} \to \text{finite} \tag{10a,b,c}$$

The initial conditions to be considered in this work are given as

$$\psi = \tilde{\psi} = \omega = \tilde{\omega} = Re = \zeta = 0, \qquad \tilde{\zeta} = 1 \tag{11a,b}$$

which correspond to the physical situation that the droplet is at rest at time $t = 0$.

3. NUMERICAL METHODS

3.1. Time discretization

One of the popular approaches for integrating the vorticity transport and the energy equations, especially in the context of spectral methods [16], has been the semi-implicit approach in which the convection terms are treated explicitly, whereas the diffusion terms are treated implicitly. In this manner, the governing equations become

$$E^2 \psi^{k+1} = -r\omega^{k+1} \sin\theta \tag{12}$$

$$\begin{aligned} &\frac{\omega^{k+1}}{\Delta t} - \frac{\Phi_v}{r \sin\theta} E^2(\omega^{k+1} r \sin\theta) \\ &= \frac{1}{\Delta t}\left[\omega^k - (Re^{k+1} - Re^k)\left(\frac{\omega}{Re}\right)^{k+1/2}\right] \\ &\quad + \frac{1}{4r}\left[3Re^k \frac{\partial(\psi^k, \omega^k/r\sin\theta)}{\partial(r,\theta)} - Re^{k-1} \frac{\partial(\psi^{k-1}, \omega^{k-1}/r\sin\theta)}{\partial(r,\theta)}\right] \end{aligned} \tag{13}$$

$$\frac{Pr}{\Delta t}\zeta^{k+1} - \Phi_\alpha \nabla^2 \zeta^{k+1} = \frac{Pr}{\Delta t}\zeta^k + \frac{1}{4r^2 \sin\theta}\left[3Pe^k \frac{\partial(\psi^k, \zeta^k)}{\partial(r,\theta)} - Pe^{k-1} \frac{\partial(\psi^{k-1}, \zeta^{k-1})}{\partial(r,\theta)}\right] \tag{14}$$

$$\left(\frac{1}{\Delta t} + \frac{3C_D^{k+1}}{16\Phi_\rho} Re^{k+1}\right) Re^{k+1} = \frac{Re^k}{\Delta t} + \Gamma \tag{15}$$

where the second-order Adams–Bashforth scheme and the backward Euler scheme have been used to integrate the convection terms and the diffusion terms respectively in the vorticity transport and the energy equations.

3.2. Galerkin spectral method

In this method, the streamfunction, the vorticity and the temperature are approximated by truncated series Legendre polynomials and their associated functions in the form

$$\{\psi^k, \tilde{\psi}^k\} = \sum_{n=1}^{NL} \{\psi_n^k, \tilde{\psi}_n^k\} \int_z^1 P_n(z^*)\, \mathrm{d}z^* \tag{16a}$$

$$\{\omega^k, \tilde{\omega}^k\} = \sum_{n=1}^{NL} \{\omega_n^k, \tilde{\omega}_n^k\} P_n^1(z) \tag{16b}$$

$$\{\zeta^k, r\tilde{\zeta}^k\} = \sum_{n=0}^{NL} \{\zeta_n^k, \tilde{\zeta}_n^k\} P_n(z) \tag{16c}$$

in which NL is the number of Legendre modes to be retained in the series, P_n and P_n^1 are the Lagendre polynomial of order n and its associated polynomial of the first kind respectively, and $z = \cos\theta$. It should be pointed out that in Equation (16c) we have chosen to expand $r\tilde{\zeta}^k$ rather than $\tilde{\zeta}^k$ so as to ease the implementation of the temperature boundary condition at the drop center.

Upon substitution of these expressions into Equations (1), (13) and (14), followed by integrating the resulting equations over the entire angular domain, there results

$$\frac{\mathrm{d}^2\psi_n^{k+1}}{\mathrm{d}r^2} - \frac{n(n+1)}{r^2}\psi_n^{k+1} = -n(n+1)r\omega_n^{k+1} \tag{17}$$

$$\frac{r^2}{\Delta t}\omega_n^{k+1} - \left[\frac{\mathrm{d}}{\mathrm{d}r}\left(r^2\frac{\mathrm{d}\omega_n^{k+1}}{\mathrm{d}r}\right) - n(n+1)\omega_n^{k+1}\right] = \frac{r^2}{\Delta t}\left[\omega_n^k - (Re^{k+1} - Re^k)\left(\frac{\omega_n}{Re}\right)^{k+1/2}\right] + \frac{1}{4}[3Re^kS_n^k - Re^{k-1}S_n^{k-1}] \tag{18}$$

$$\frac{Pr}{\Delta t}(r^2\zeta_n^{k+1}) - \left[\frac{\mathrm{d}}{\mathrm{d}r}\left(r^2\frac{\mathrm{d}\zeta_n^{k+1}}{\mathrm{d}r}\right) - n(n+1)\zeta_n^{k+1}\right] = \frac{Pr}{\Delta t}(r^2\zeta_n^k) + \frac{1}{4}[3Pe^kH_n^k - Pe^{k-1}H_n^{k-1}] \tag{19}$$

$$\frac{\mathrm{d}^2\tilde{\psi}_n^{k+1}}{\mathrm{d}r^2} - \frac{n(n+1)}{r^2}\tilde{\psi}_n^{k+1} = -n(n+1)r\tilde{\omega}_n^{k+1} \tag{20}$$

$$\frac{r^2}{\Delta t}\tilde{\omega}_n^{k+1} - \Phi_v\left[\frac{\mathrm{d}}{\mathrm{d}r}\left(r^2\frac{\mathrm{d}\tilde{\omega}_n^{k+1}}{\mathrm{d}r}\right) - n(n+1)\tilde{\omega}_n^{k+1}\right] = \frac{r^2}{\Delta t}\left[\tilde{\omega}_n^k - (Re^{k+1} - Re^k)\left(\frac{\tilde{\omega}_n}{Re}\right)^{k+1/2}\right] + \frac{1}{4}[3Re^k\tilde{S}_n^k - Re^{k-1}\tilde{S}_n^{k-1}] \tag{21}$$

$$\frac{Pr}{\Delta t}(r^2\tilde{\zeta}_n^{k+1}) - \Phi_\alpha\left[r^2\frac{\mathrm{d}^2\tilde{\zeta}_n^{k+1}}{\mathrm{d}r^2} - n(n+1)\tilde{\zeta}_n^{k+1}\right] = \frac{Pr}{\Delta t}(r^2\tilde{\zeta}_n^{k}) + \frac{1}{4}[3Pe^k\tilde{H}_n^k - Pe^{k-1}\tilde{H}_n^{k-1}] \tag{22}$$

where S_n, $\tilde{S}_n$, H_n and $\tilde{H}_n$ represent

$$S_n = -\sum_{i=1}^{NL}\sum_{j=1}^{NL}\left\{a_{ij}^n\psi_i\left(\frac{\mathrm{d}\omega_j}{\mathrm{d}r} - \frac{\omega_j}{r}\right) + b_{ij}^n\frac{\mathrm{d}\psi_i}{\mathrm{d}r}\omega_j\right\} \tag{23}$$

$$\tilde{S}_n = -\sum_{i=1}^{NL}\sum_{j=1}^{NL}\left\{a_{ij}^n\tilde{\psi}_i\left(\frac{\mathrm{d}\tilde{\omega}_j}{\mathrm{d}r} - \frac{\tilde{\omega}_j}{r}\right) + b_{ij}^n\frac{\mathrm{d}\tilde{\psi}_i}{\mathrm{d}r}\tilde{\omega}_j\right\} \tag{24}$$

$$H_n = -\sum_{i=1}^{NL}\sum_{j=0}^{NL}\left\{c_{ij}^n\psi_i\frac{\mathrm{d}\zeta_j}{\mathrm{d}r} + d_{ij}^n\frac{\mathrm{d}\psi_i}{\mathrm{d}r}\zeta_j\right\} \tag{25}$$

$$\tilde{H}_n = -\sum_{i=1}^{NL}\sum_{j=0}^{NL}\left\{c_{ij}^n\tilde{\psi}_i\left(\frac{\mathrm{d}\tilde{\zeta}_j}{\mathrm{d}r} - \frac{\tilde{\zeta}_j}{r}\right) + d_{ij}^n\frac{\mathrm{d}\tilde{\psi}_i}{\mathrm{d}r}\tilde{\zeta}_j\right\} \tag{26}$$

with the coefficients a_{ij}^n, b_{ij}^n, c_{ij}^n and d_{ij}^n defined as

$$a_{ij}^n = \frac{2n+1}{2n(n+1)}\int_{-1}^{1} P_n^1P_iP_j^1\,\mathrm{d}z, \qquad b_{ij}^n = \frac{2n+1}{2n(n+1)}\int_{-1}^{1} P_n^1P_i^1P_j^2\,\mathrm{d}z \tag{27a,b}$$

$$c_{ij}^n = \frac{2n+1}{2}\int_{-1}^{1} P_nP_iP_j\,\mathrm{d}z, \qquad d_{ij}^n = \frac{2n+1}{2j(j+1)}\int_{-1}^{1} P_nP_i^1P_j^1\,\mathrm{d}z \tag{27c,d}$$

which were evaluated numerically by means of a Gaussian quadrature formula.

3.3. Spectral element method

To adapt a spectral element method, the radial domain is divided into a finite number of elements, say E. Within each element, each component of the streamfunction, vorticity and temperature at any time level (with the superscript k omitted) are expanded as linear combinations of a set of basis functions as

$$\psi_n^e = \sum_{m=0}^{N^e}\psi_{nm}^e w_m(\xi), \qquad \omega_n^e = \sum_{m=0}^{N^e}\omega_{nm}^e w_m(\xi), \qquad \zeta_n^e = \sum_{m=0}^{N^e}\zeta_{nm}^e w_m(\xi) \tag{28a,b,c}$$

where N^e+1 is the number of degrees of freedom per element, ξ is the local element co-ordinate and ψ_{nm}^e, ω_{nm}^e and ζ_{nm}^e are the values of the corresponding variables at the point ξ_m, selected to be the Gauss–Lobatto quadrature points, i.e. $\xi_m = \cos(m\pi/N^e)$, and the $w_m(\xi)$ are the Lagrangian interpolants of the form

$$w_m(\xi) = \frac{2}{N^e}\sum_{m'=0}^{N^e}\frac{1}{\bar{d}_m\bar{d}_{m'}}T_{m'}(\xi_m)T_{m'}(\xi) \tag{29}$$

in which $T_m(\xi)$ is the Chebyshev polynomial of order m and $\bar{d}_m$ is a parameter that has a value of 2 if $m=0$ or N^e, and 1 otherwise. Without much effort, this function can be shown to possess a property that $w_m^e(\xi_k)=\delta_{mk}$ where δ_{mk} is the Kronecker delta.

Following the Galerkin procedure, residuals of Equations (17)–(22) are formed and are then orthogonal to each member of the set of basis function so as to minimize the residuals. The discrete analogs of Equation (17)–(22) are then

$$\sum_{e=1}^{E}([A]^e+n(n+1)[B]^e)\{\psi_n^{k+1}\}^e=\sum_{e=1}^{E}\{F\omega_n\}^e \tag{30}$$

$$\sum_{e=1}^{E}([A]^e+n(n+1)[B]^e)\{\tilde{\psi}_n^{k+1}\}^e=\sum_{e=1}^{E}\{F\tilde{\omega}_n\}^e \tag{31}$$

$$\sum_{e=1}^{E}\left(\frac{1}{\Delta t}[C]^e+[D]^e+n(n+1)[B]^e\right)\{\omega_n^{k+1}\}^e=\sum_{e=1}^{E}\{FS_n\}^e \tag{32}$$

$$\sum_{e=1}^{E}\left(\frac{1}{\Delta t}[C]^e+\Phi_v([D]^e+n(n+1)[B]^e)\right)\{\tilde{\omega}_n^{k+1}\}^e=\sum_{e=1}^{E}\{F\tilde{S}_n\}^e \tag{33}$$

$$\sum_{e=1}^{E}\left(\frac{Pr}{\Delta t}[C]^e+[D]^e+n(n+1)[B]^e\right)\{\zeta_n^{k+1}\}^e=\sum_{e=1}^{E}\{FH_n\}^e \tag{34}$$

$$\sum_{e=1}^{E}\left(\frac{Pr}{\Delta t}[C]^e+\Phi_\alpha([A]^e+n(n+1)[B]^e)\right)\{\tilde{\zeta}_n^{k+1}\}^e=\sum_{e=1}^{E}\{F\tilde{H}_n\}^e \tag{35}$$

where the components of the element matrices are given by

$$[A]_{ij}^e=\frac{8}{L^e(N^e)^2}\sum_{i'=0}^{N^e}\sum_{j'=0}^{N^e}\frac{T_{i'}(\xi_i)T_{j'}(\xi_j)}{\bar{d}_{i'}\bar{d}_i\bar{d}_{j'}\bar{d}_j}\int_{-1}^{1}\frac{\mathrm{d}(r^2T_{i'})}{\mathrm{d}\xi}\frac{\mathrm{d}(T_{j'})}{\mathrm{d}\xi}\,\mathrm{d}\xi \tag{36a}$$

$$[B]_{ij}^e=\frac{2L^e}{(N^e)^2}\sum_{i'=0}^{N^e}\sum_{j'=0}^{N^e}\frac{T_{i'}(\xi_i)T_{j'}(\xi_j)}{\bar{d}_{i'}\bar{d}_i\bar{d}_{j'}\bar{d}_j}\int_{-1}^{1}T_{i'}T_{j'}\,\mathrm{d}\xi \tag{36b}$$

$$[C]_{ij}^e=\frac{2L^e}{(N^e)^2}\sum_{i'=0}^{N^e}\sum_{j'=0}^{N^e}\frac{T_{i'}(\xi_i)T_{j'}(\xi_j)}{\bar{d}_{i'}\bar{d}_i\bar{d}_{j'}\bar{d}_j}\int_{-1}^{1}r^2T_{i'}T_{j'}\,\mathrm{d}\xi \tag{36c}$$

$$[D]_{ij}^e=\frac{8}{L^e(N^e)^2}\sum_{i'=0}^{N^e}\sum_{j'=0}^{N^e}\frac{T_{i'}(\xi_i)T_{j'}(\xi_j)}{\bar{d}_{i'}\bar{d}_i\bar{d}_{j'}\bar{d}_j}\int_{-1}^{1}r^2\frac{\mathrm{d}T_{i'}}{\mathrm{d}\xi}\frac{\mathrm{d}T_{j'}}{\mathrm{d}\xi}\,\mathrm{d}\xi \tag{36d}$$

With the aid of the recursive formulae and the product rule of Chebyshev polynomials, the integrals in Equations (36a)–(36d) can be computed exactly. Further details can be found in the monograph by Fox and Parker [17].

4. INFLUENCE MATRIX TECHNIQUE

The major advantage of the influence matrix technique lies in its effectiveness to alleviate the difficulty associated with the lack of the vorticity boundary conditions. As will be demonstrated shortly, it is also a useful tool for removing the couplings between the two phases, thereby allowing the equations in each phase to be solved independently. The key idea of this method is to express the solution as a linear combination of the solutions of simpler but related problems. For the flow we propose the following decomposition:

$$\begin{Bmatrix} \psi_n^{k+1} \\ \omega_n^{k+1} \\ \tilde{\psi}_n^{k+1} \\ \tilde{\omega}_n^{k+1} \end{Bmatrix} = \begin{Bmatrix} f_0 \\ g_0 \\ \tilde{f}_0 \\ \tilde{g}_0 \end{Bmatrix} + \phi_1 \begin{Bmatrix} f_1 \\ g_1 \\ 0 \\ 0 \end{Bmatrix} + \phi_2 \begin{Bmatrix} 0 \\ 0 \\ \tilde{f}_1 \\ \tilde{g}_1 \end{Bmatrix} \tag{37}$$

where ϕ_1 and ϕ_2 are constant coefficients to be determined. The auxiliary functions introduced in Equation (37) are the solutions of the following problems:

$$\begin{cases} \dfrac{(r^2 g_1)}{\Delta t} - \left[\dfrac{\partial}{\partial r}\left(r^2 \dfrac{\partial g_1}{\partial r} \right) - n(n+1) g_1 \right] = 0 \\ \dfrac{\partial^2 f_1}{\partial r^2} - n(n+1) f_1 = -n(n+1) g_1 \\ \text{subjected to } g_1(\infty) = 0, \quad g_1(1) = 1, \quad f_1(\infty) = 0, \quad f_1(1) = 0 \end{cases} \tag{38}$$

$$\begin{cases} \dfrac{(r^2 \tilde{g}_1)}{\Delta t} - \Phi_v \left[\dfrac{\partial}{\partial r}\left(r^2 \dfrac{\partial \tilde{g}_1}{\partial r} \right) - n(n+1) \tilde{g}_1 \right] = 0 \\ \dfrac{\partial^2 \tilde{f}_1}{\partial r^2} - n(n+1) \tilde{f}_1 = -n(n+1) \tilde{g}_1 \\ \text{subjected to } \tilde{g}_1(1) = 1, \quad \tilde{g}_1(0) = 0, \quad \tilde{f}_1(1) = 0, \quad f_1(0) = 0 \end{cases} \tag{39}$$

$$\begin{cases} \dfrac{(r^2 g_0)}{\Delta t} - \left[\dfrac{\partial}{\partial r}\left(r^2 \dfrac{\partial g_0}{\partial r} \right) - n(n+1) g_0 \right] \\ \quad = \dfrac{r^2}{\Delta t} \left[\omega_n^k - (Re^{k+1} - Re^k) \left(\dfrac{\omega}{Re} \right)^{k+1/2} \right] + \dfrac{1}{4} [3 Re^k S_n^k - Re^{k-1} S_n^{k-1}] \\ \dfrac{\partial^2 f_0}{\partial r^2} - n(n+1) f_0 = -n(n+1) g_0 \\ \text{subjected to } g_0(\infty) = 0, \quad g_0(1) = 0, \quad f_0(\infty) \to r^2 \delta_{n1}, \quad f_0(1) = 0 \end{cases} \tag{40}$$

$$\begin{cases} \dfrac{(r^2\tilde{g}_0)}{\Delta t} - \Phi_v\left[\dfrac{\partial}{\partial r}\left(r^2\dfrac{\partial \tilde{g}_0}{\partial r}\right) - n(n+1)\tilde{g}_0\right] \\ \quad = \dfrac{r^2}{\Delta t}\left[\tilde{\omega}_n^k - (Re^{k+1} - Re^k)\left(\dfrac{\tilde{\omega}_n}{Re}\right)^{k+1/2}\right] + \dfrac{1}{4}[3Re^k\tilde{S}_n^k - Re^{k-1}\tilde{S}_n^{k-1}] \\ \dfrac{\partial^2\tilde{f}_0}{\partial r^2} - n(n+1)\tilde{f}_0 = -n(n+1)\tilde{g}_0 \\ \text{subjected to } \tilde{g}_0(1) = 0, \quad \tilde{g}_0(0) = 0, \quad \tilde{f}_0(1) = 0, \quad \tilde{f}_0(0) = 0 \end{cases} \tag{41}$$

Having defined the auxiliary functions, the decomposition coefficients are determined from the continuity in tangential velocity and shear stresses. This yields two equations to be solved for ϕ_1 and ϕ_2 given in matrix form as

$$\begin{bmatrix} f_1' & -\tilde{f}_1' \\ f_1'' - 2f_1' & \Phi_\mu(\tilde{f}_1'' - 2\tilde{f}_1') \end{bmatrix}\begin{Bmatrix}\phi_1 \\ \phi_2\end{Bmatrix} = \begin{Bmatrix} \tilde{f}_0' - f_0' \\ \Phi_\mu(\tilde{f}_0'' - 2\tilde{f}_0') - (f_0'' - 2f_0')\end{Bmatrix} \tag{42}$$

where the prime indicates the derivative with respect to r.

Similarly, the energy equation can be decoupled by the use of the following decomposition:

$$\begin{Bmatrix}\zeta_n^{k+1} \\ \tilde{\zeta}_n^{k+1}\end{Bmatrix} = \begin{Bmatrix}h_0 \\ \tilde{h}_0\end{Bmatrix} + \sigma_1\begin{Bmatrix}h_1 \\ 0\end{Bmatrix} + \sigma_2\begin{Bmatrix}0 \\ \tilde{h}_1\end{Bmatrix} \tag{43}$$

where σ_1 and σ_2 are again the two constants to be determined. The associated auxiliary problems for temperature are

$$\begin{cases} Pr\dfrac{(r^2h_1)}{\Delta t} - \left[\dfrac{\partial}{\partial r}\left(r^2\dfrac{\partial h_1}{\partial r}\right) - n(n+1)h_1\right] = 0 \\ \text{with } h_1(1) = 1 \quad \text{and} \quad h_1(\infty) = 0 \end{cases} \tag{44}$$

$$\begin{cases} Pr\dfrac{(r^2\tilde{h}_1)}{\Delta t} - \Phi_\alpha\left[r^2\dfrac{\partial^2\tilde{h}_1}{\partial r^2} - n(n+1)\tilde{h}_1\right] = 0 \\ \text{with } \tilde{h}_1(0) = 0 \quad \text{and} \quad \tilde{h}_1(1) = 1 \end{cases} \tag{45}$$

$$\begin{cases} \dfrac{Pr}{\Delta t}(r^2h_0) - \left[\dfrac{\partial}{\partial r}\left(r^2\dfrac{\partial h_0}{\partial r}\right) - n(n+1)h_0\right] = \dfrac{Pr}{\Delta t}(r^2\zeta_n^k) + \dfrac{1}{4}[3Pe^kH_n^k - Pe^{k-1}H_n^{k-1}] \\ \text{subjected to } h_0(1) = 0 \quad \text{and} \quad h_0(\infty) = 0 \end{cases} \tag{46}$$

$$\begin{cases} Pr\dfrac{(r^2\tilde{h}_0)}{\Delta t} - \Phi_\alpha\left[r^2\dfrac{\partial^2\tilde{h}_0}{\partial r^2} - n(n+1)\tilde{h}_0\right] = \dfrac{Pr}{\Delta t}(r^2\tilde{\zeta}_n^k) + \dfrac{1}{4}[3Pe^k\tilde{H}_n^k - Pe^{k-1}\tilde{H}_n^{k-1}] \\ \text{subjected to } \tilde{h}_1(0) = 0 \quad \text{and} \quad \tilde{h}_1(1) = 0 \end{cases} \tag{47}$$

From the continuity of temperature and heat flux at the interface, we arrive at the equation for calculating the decomposition coefficients σ_1 and σ_2,

$$\begin{bmatrix} 1 & -1 \\ h_1' & \Phi_\kappa(\tilde{h}_1' - 1) \end{bmatrix}\begin{Bmatrix}\sigma_1 \\ \sigma_2\end{Bmatrix} = \begin{Bmatrix} 0 \\ \Phi_\kappa\tilde{h}_0' - h_0' \end{Bmatrix} \tag{48}$$

A careful assessment of the above procedure indicates that only Equations (40), (41), (46) and (47) need to be solved at each time step. In view of this, the influence matrix technique is indeed an effective strategy to deal with the complications arising from the overspecification of the streamfunction and the underspecification of the vorticity boundary conditions and the two-phase interactions without added computational burden.

5. PHYSICAL QUANTITIES

Two of the most important parameters in the study of particle transport phenomena are the total drag force acting on the particle and the heat transfer rate as represented by the Nusselt number. For a drop experiencing no interfacial mass transfer, the total drag force is the sum of the form drag, D_f, and the pressure drag, D_p, components computed from

$$D_f = 2\pi R^2\int_0^\pi (-\tau_{r\theta}|_{r=1}\sin\theta + \tau_{rr}|_{r=1}\cos\theta)\sin\theta\,\mathrm{d}\theta \tag{49a}$$

$$D_p = -2\pi R^2\int_0^\pi \Pi|_{r=1}\sin\theta\cos\theta\,\mathrm{d}\theta \tag{49b}$$

where Π is the pressure that can be found from the θ component of the momentum equation and $\tau_{r\theta}$ and τ_{rr} are the tangential and normal components of the stress tensor respectively. Since a derivation of an expression for the pressure is straightforward, details are omitted. By integrating the pressure and the stresses as indicated in (49a) and (49b) and normalizing the results with the dynamic head ($\pi\rho U_p^2R^2/2$) yields the drag coefficient

$$C_D = \frac{16}{3Re}(\omega_1'|_{r=1} - \omega_1|_{r=1}) + 8\sum_{n=1}^{NL}\frac{\psi_n'|_{r=1}\psi_{n+1}'|_{r=1}}{(2n+3)(n+1)(2n+1)} - \frac{8}{3Re}\left[\frac{\mathrm{d}\psi_1'|_{r=1}}{\mathrm{d}t} + \left(\frac{\psi_1'|_{r=1}}{Re}\right)\frac{\mathrm{d}Re}{\mathrm{d}t}\right] \tag{50}$$

which can easily be evaluated once the streamfunction and vorticity components are known. At steady state, the terms in the square bracket vanish; hence Equation (50) reduces to the expression given in Oliver and Chung [7].

Using the definition adopted by Oliver and Chung [10], the instantaneous Nusselt number, *Nu*, can be computed from

$$Nu = -\frac{2}{\tilde{\zeta}_b}\zeta'_0\big|_{r=1} \tag{52}$$

where $\tilde{\zeta}_b$ is the dimensionless bulk temperature given by

$$\tilde{\zeta}_b = \frac{3}{2}\int_0^{\pi}\int_0^1 \tilde{\zeta} r^2 \sin\theta \, dr \, d\theta \tag{51}$$

As to be discussed in the next section, the lack of appropriate data for a comprehensive numerical assessment of the present numerical method further signifies the role of these quantities. Consequently, the drag coefficient and the Nusselt number are used extensively to validate the numerical model.

6. RESULTS AND DISCUSSION

Several issues need to be considered in this section. Perhaps, the most critical of all is a demonstration of the preservation of spectral accuracy. Fortunately, this has been demonstrated by Patera [13] as he showed in Cartesian co-ordinate that the absolute error decreases in an exponential fashion as the number of degrees of freedom increases; hence, no attempt is made to reexamine it again in this study. Rather, evaluation of the above numerical model is based on how well it is able to match previously reported results. In addition, results are presented for droplet evolution including interfacial properties.

Direct comparison of results as computed here with those in the literature is possible only in the special situation of constant free stream velocity. Table I summarizes the comparison between our predicted drag coefficient with those of Oliver and Chung [7] and Rivkind *et al.* [18] for Reynolds numbers from 0.5 to 50 at three viscosity ratios (0.333, 1 and 3). In general, the agreement is very good, being about 7% below the values of Oliver and Chung, and slightly more than 3% below those of Rivkind *et al.* Even though no conclusion can be drawn as to which method is the best, they agree to within numerical errors. Next, we examine the tangential velocity along the drop surface for $Re = 50$ with viscosity ratios of 0.333 and 3. From Figure 2, it is apparent that the two numerical models predict similar profiles. However, the magnitude tends to be off as much as 10% near the pole, where it exhibits a maximum value.

In an attempt to provide more confidence in our results, we shall turn our attention to the experimental data of Abdel-Alim and Hamielec [19] for a drop in a liquid and of Elzinga and Banchero [20] for a solid sphere. For the liquid–liquid systems, the experiments

Table I. Comparison of predicted drag coefficients with $\Phi_\rho = \Phi_\mu$.

Φ_μ	Re					Reference
	0.5	1	5	20	50	
0.333	38.1	19.9	4.89	1.70	0.86	Present
	38.2	20.0	5.02	1.74	0.90	[7]
	38.3	19.9	4.89	1.71	0.89	[18]
1	42.6	22.3	5.61	2.00	1.12	Present
	42.7	22.5	5.75	2.09	1.15	[7]
	42.9	22.4	5.65	2.05	1.12	[18]
3	47.3	24.8	6.33	2.37	1.34	Present
	47.2	25.0	6.50	2.45	1.44	[7]
	47.4	24.8	6.36	2.38	1.36	[18]

were set up in such a way that the dispersed phase is water, whereas the continuous phase is cyclohexanol and *n*-butyl lactate. As such, the density ratio was approximately unity while the viscosity ratio was manipulated by adding a small amount of carboxymethyl cellulose to the water drop. Table II presents our drag coefficients along with the experimental data. Clearly, the agreement is acceptable but it is not quite as good as before. One possible explanation for this discrepancy is the surface contamination that would cause a surface tension variation, which in turn may alter the pressure and stresses distribution along the interface. A careful examination of their data, particularly for $Re = 5$, reveals an unusual behavior in the drag coefficients. Instead of the drag coefficient being an increasing function of the viscosity ratio their data show an irregular dependence on Φ_μ; thereby suggesting the possibility of the presence of such effects. This phenomenon, known as Marangoni convection, is not new and has been shown to produce significant effects depending on the Marangoni number [21]. Because the information necessary for computing this dimensionless number was not given in Reference [19], it is difficult to justify whether or not such effects are indeed negligible.

As for heat transfer, assessment of the results becomes more difficult because the internal circulation inside the drop causes the Nusselt number to oscillate in time unless Φ_μ is large. Thus, we shall use the limiting case of heat transfer about a solid sphere. Table III compares the Nusselt numbers for a sphere at $Re = 20$, in a fluid having $Pr = 15$, and $\Phi_\alpha = 1$ for three different thermal conductivity ratios: 0.333, 1 and 3. Again, the data agree quite well with those of ours [11] and Oliver and Chung [10]. Also compared is the local Nusselt number as a function of the angular co-ordinate as illustrated in Figure 3. With the exception of the vicinity of the front stagnation point, our predicted local Nusselt number is nearly identical to the data of Oliver and Chung [10]. Beyond this region, pronounced deviations occur and by being underpredicted, our results better match the experimental data of Froessling [22].

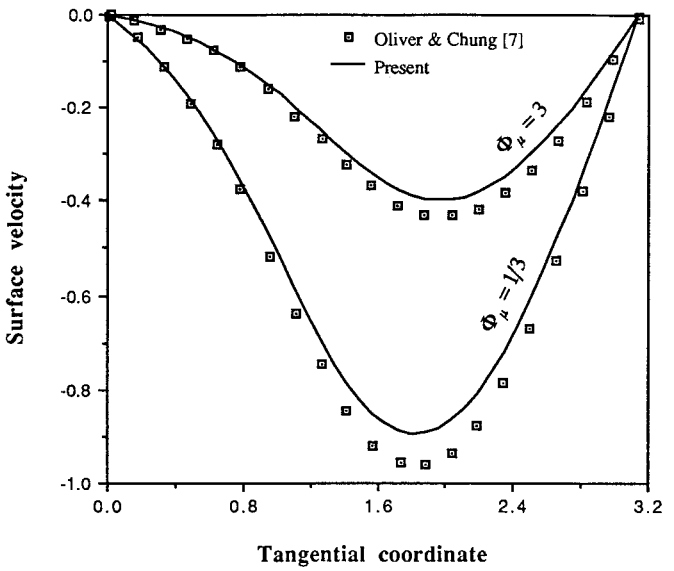

Figure 2. Comparison of surface velocity for $Re = 50$ and $\Phi_\rho = 1$.

Table II. Comparison of drag coefficients with experiment with $\Phi_\rho = 1$.

Φ_μ	Re					Reference
	1	5	10	25	50	
0.0995	18.3	4.5	2.6	—	—	Present
	18.0	4.6	2.8	—	—	[19]
0.266	—	4.89	—	1.39	0.80	Present
	—	4.5	—	1.45	0.9	[19]
0.301	19.7	4.95	2.9	—	—	Present
	19.0	5.0	3.1	—	—	[19]
0.554	20.9	5.21	3.1	—	—	Present
	20.0	5.2	3.3	—	—	[19]
0.708	—	5.34	—	1.61	0.98	Present
	—	4.9	—	1.75	1.2	[19]
1.4	—	5.85	—	1.84	1.18	Present
	—	5.0	—	1.8	1.25	[19]
∞	—	—	4.2	—	1.53	Present
	—	—	4.5	—	1.65	[20]

Table III. Comparison of Nusselt number ($Re = 20$, $Pr = 15$, $\Phi_\alpha = 1$ and $\Phi_\mu = \infty$).

Φ_κ	Present	Nguyen *et al.* [11]	Oliver and Chung [10]
0.333	1.91	1.91	1.84
1.0	4.10	4.12	4.08
3.0	6.77	6.81	6.72

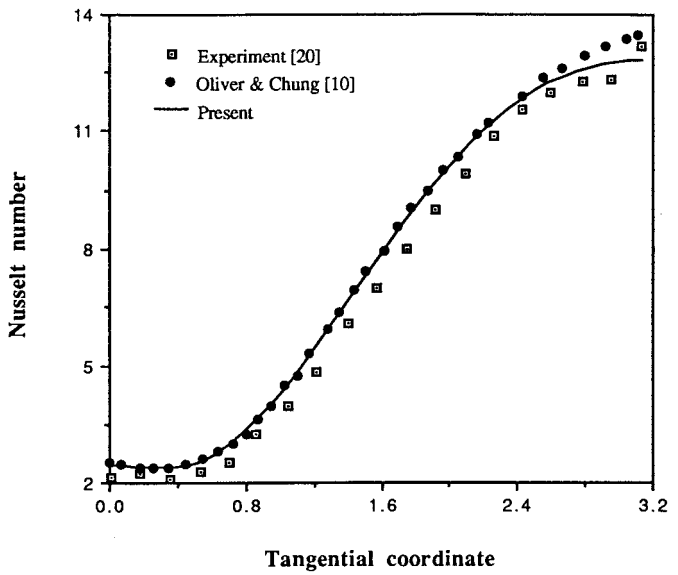

Figure 3. Comparison of local Nusselt number ($Re = 48$, $Pr = 2.5$, $\Phi_\alpha = 1$, $\Phi_\kappa = 100$ and $\Phi_\mu = 10^7$).

Despite the success demonstrated in the preceding paragraphs, the imperfect match of the data necessitates a convergence analysis. Tables IV and V show the drag coefficient as a function of the truncation radius and the number of Legendre functions respectively. As one can see, only a few Legendre functions, as low as three for $Re = 1$, are needed at low Reynolds number and this number increases to somewhere between 15 and 20 for a Reynolds number of 300. In contrast to NL, the truncation radius becomes very large as the Reynolds number approaches zero. This is not surprising, but is in fact consistent with the boundary layer analysis that predicts this distance to be theoretically infinite. For all of the results tabulated in Tables I and II, r_∞ was truncated at 100 for all Re whereas NL varies from 5 for $Re \leq 10$ to 10 for $10 \leq Re \leq 25$ and to 15 for $Re = 50$. For the sensitivity study of the drag coefficient

Table IV. Effects of r_∞ drag coefficient ($\Phi_\rho = 790$ and $\Phi_\mu = 55$).

Re	r_∞				
	30	50	100	150	200
1[a]	25.62	26.23	26.76	26.96	27.04
100[b]	1.01	1.05	1.08		

[a] $NL = 3$.
[b] $NL = 15$.

Table V. Effects of NL on drag coefficient ($\Phi_\rho = 790$, $\Phi_\mu = 55$ and $r_\infty = 100$).

Re	*NL*				
	3	5	10	15	20
1	26.76	26.79			
100	0.692	0.780	1.10	1.08	1.08
300	0.362	0.461	0.701	0.630	0.662

on the number of elements, Table VI shows the calculated drag coefficient variation. As shown in Table VI, the drag coefficient is less sensitive to the number of elements than NL. In all the calculations, a variable grid of 40 elements was used in the continuous phase with the same number used in a similar fashion in the dispersed phase. In order to avoid excessive computations, we minimize the bandwidth of the global matrix by adopting a value of 2 for N^e. On the basis of our convergence study, this choice of values seems to be justifiable.

Proceeding to the dynamics of an accelerating droplet in a non-isothermal medium, one may recall that the flow and temperature fields associated with an accelerating droplet can only be completely dictated once the following model parameters are specified: Pr, Γ ($= (2gR^3/v^2)(1 - (1/\Phi_\rho))$, the right-hand side of Equation (6)) Φ_ρ, Φ_μ, Φ_κ and Φ_α. Thus, a parametric study covering all the possible combinations among these parameters is beyond the scope of this

Table VI. Effects of number of element on drag coefficient ($\Phi_\rho = 790$, $\Phi_\mu = 55$, $NL = 15$ and $r_\infty = 100$).

Re	Number of element				
	20	30	40	100	200
100	26.31	26.64	26.76	26.76	26.77
300	0.573	0.612	0.630	0.632	0.632

study. We instead concentrate on a particular system involving a water drop falling in an otherwise stagnant air having $Pr = 0.7$, $\Phi_\rho = 680$, $\Phi_\mu = 24.6$, $\Phi_\kappa = 7.5$ and $\Phi_\alpha = 4.1 \times 10^{-3}$. Figure 4(a)–(c) depict the streamlines and the temperature contours for $\Gamma = 0.3$ at $t = 50$, 100 and 600 respectively. The flow patterns are quite similar to that of a solid sphere except that an internal motion in the form of Hill's spherical vortex now exists due to the imbalance of the shear stress at the drop surface. Even after 50 elapsed time units, a large degree of symmetry about the equatorial plane still persists. As time increases, the flow separates from the droplet and the wake develops into a recirculation zone, within which the flow intensity is very small compared with that in the main flow. Such a secondary flow is initially confined in a small region around the rear stagnation point, but grows in time continuously until steady state at which the wake length is approximately 0.8 times the droplet radius. For the temperature, the fluid motion causes the isotherms to deform in such a way that those outside the drop elongate in the streamwise direction and those inside the drop form a kidney-like shape. In contrast to the streamlines, rapid temperature development occurred in the early stage, during which the isotherms evolve from circular shape to those illustrated in Figure 4(a), where no trace of spherical symmetry remains. Although the structure of the temperature field stays very much unchanged, as indicated in these figures, it by no means implies a steady state is reached since the isotherms have been scaled by the droplet bulk temperature. In fact, from the cooling history, the droplet bulk temperature is seen to drop from a value of 0.818 at $t = 50$ to 0.028 at $t = 600$.

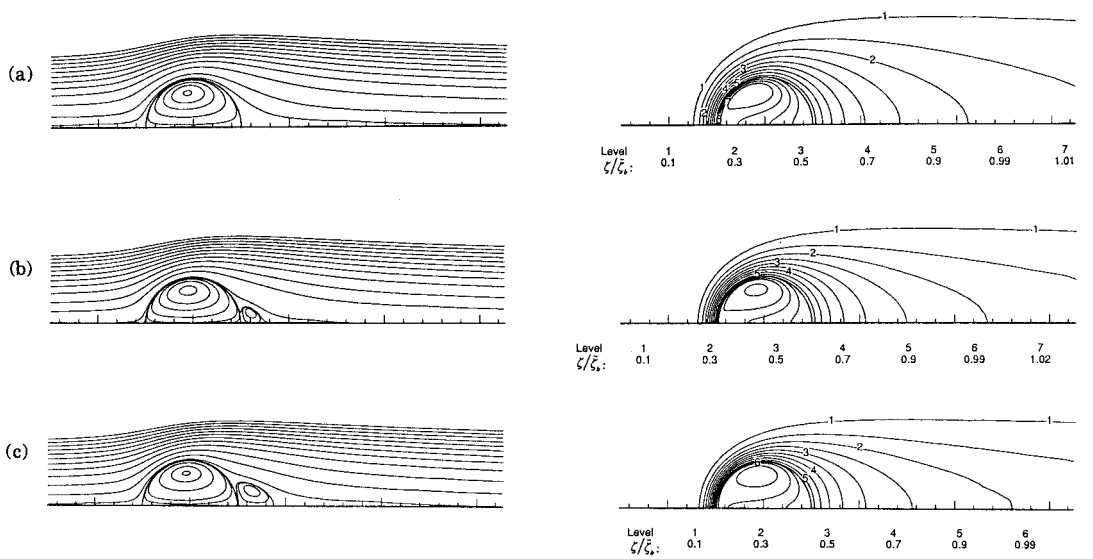

Figure 4. Temporal development of flow (left) and temperature (right) fields for $\Gamma = 0.3$: (a) $t = 50$, (b) $t = 100$, (c) $t = 600$.

Figure 5(a)–(d) provides additional information about the evolution of the transport process of the above air–water droplet system by plotting the surface velocity, vorticity, temperature and Nusselt number versus angular co-ordinate for three different times corresponding to those illustrated in Figure 4. Clearly, the interfacial velocity, hence the strength of the internal circulation, increases with time and behaves in a manner consistent with that of a droplet translating at a constant speed. At first glance, these values seem small, but they are reasonable considering the large viscosity of water compared with air ($\Phi_\mu = 24.6$). With that small velocity, it is a dominant mechanism of momentum transfer in the droplet owing to the high Prandtl number of water. As for the surface vorticity, (Figure 5(b)), the changes are rather small in the wake as opposed to the main flow where the variations are much more drastic. Prior to flow separation, the surface vorticity profile exhibits a monotonic behavior. But as

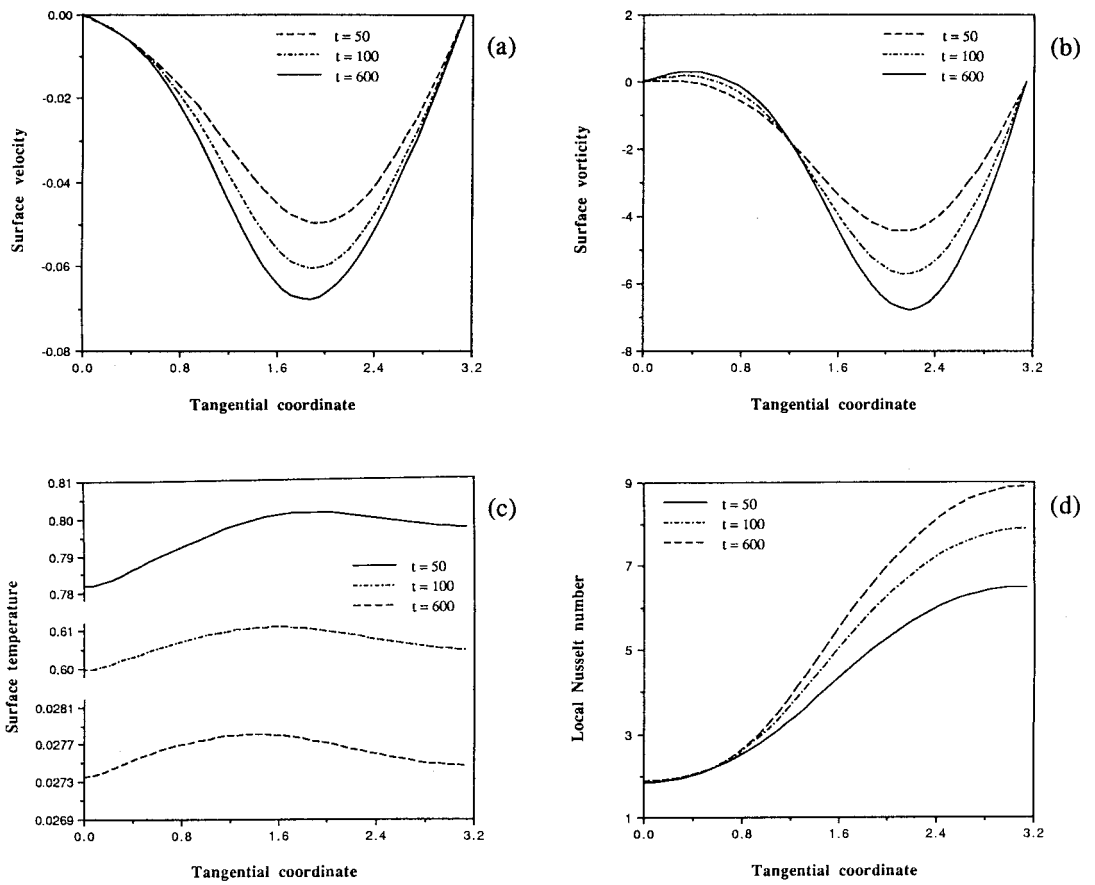

Figure 5. Evolution of interfacial quantities for $\Gamma = 0.3$: (a) surface velocity, (b) surface vorticity, (c) surface temperature, (d) local Nusselt number.

soon as the flow separates from the drop surface, the curvature changes such that the surface vorticity becomes positive in the wake. One of the unique features of transport associated with a droplet is the internal mixing effects which have caused the surface temperature to become more uniform than that of a solid sphere [23]. A careful examination of the surface temperature (Figure 5(c)) and the heat flux (Figure 5(d)) reveals a displacement of the maximum temperature location from the pole to near the equator. This phenomenon is attributed to the internal mixing.

To illustrate the effects of the initial acceleration on droplet histories, the time variations of the droplet velocity, the droplet bulk temperature and the overall Nusselt number are given in Figure 6(a)–(c) respectively for several values of Γ, ranging from 0.01 to 0.3. In general, the larger the initial acceleration the shorter the time required for the droplet to attain its terminal velocity, the faster the cooling, and hence the higher the beat transfer rate. Also observed in these figures is a strong dependence of the droplet terminal velocity and the steady state Nusselt number on the initial acceleration, which is as expected. Because a larger initial acceleration means stronger convection, the steady state Nusselt number is higher for larger Γ. Perhaps the most interesting thing about the Nusselt number history is its non-monotonicity in that the Nusselt number decreases rapidly to a minimum value, then increases to the steady state limit. Since this event is absent from the Nusselt number history for a solid sphere, it is possibly due to the mixing of fresh and warm fluids inside the droplet. A comparison of the steady state Nusselt numbers agrees well with Equations (5)–(25) of Clift *et al.* [21] as one would anticipate.

7. SUMMARY AND CONCLUSIONS

A spectral numerical method has been developed to combine various useful features of the spectral Galerkin method and the Galerkin-based spectral element method. Validation has been carried out on a two-phase transport test problem involving a hot liquid droplet undergoes heat transfer with the surrounding air while falling under gravity. A summary of conclusions is given below.

1. The results predicted by the present method compared well with previous studies as well as with experimental data.
2. For a fixed total number of nodal points used in the radial direction the present Legendre-spectral element method yielded banded matrices as opposed to full matrices produced by a pseudo-spectral method.
3. For a fixed total number of nodal points in the radial direction the partition of the elements provided an additional degree of flexibility for better resolve stiff gradients at the interface.
4. The influence matrix technique was very effective to decouple the phasic interactions at the interface and to case the difficulty in specifying the vorticity boundary conditions without added computational burden.

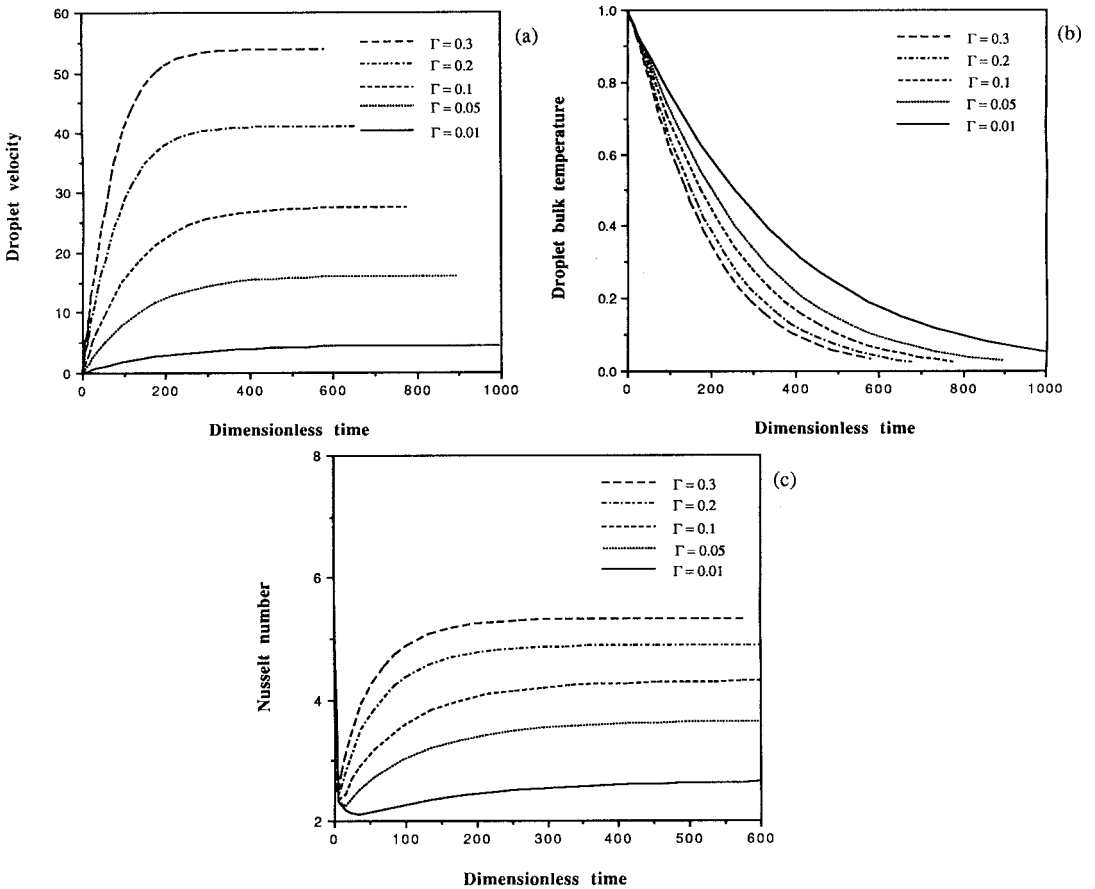

Figure 6. Droplet histories: (a) droplet velocity, (b) bulk temperature, (c) Nusselt number.

REFERENCES

1. Hadamard J. Movement permanent lent d'une sphere liquide et visqueuse dans un liquid visqueux. *Comptes Rendus de l'Academie des Sciences* 1911; **152**: 1735–1738.
2. Rybczynski W. Uber die fortschreitende bewegung einer flussigen kugel in einem zaben medium. *Bulletin of the International Academy of Poland Science Letters, Class of Science, Mathematics and Nature, Series A* 1911; **40**.
3. Chao BT. Motion of spherical gas bubbles in a viscous liquid at large Reynolds numbers. *Physics in Fluids* 1962; **5**: 69–79.
4. Taylor TD, Acrivos A. On the deformation and drag of a falling viscous drop at low Reynolds number. *Journal of Fluid Mechanics* 1964; **18**: 466.
5. LeClair BP, Hamielec AE, Pruppacher HR, Hall WD. A theoretical and experimental study of the internal circulation in water drops falling at terminal velocity in air. *Journal of Atmospheric Science* 1972; **29**: 728–740.
6. Oliver DLR, Chung JN. Steady flows inside and around a fluid sphere at low Reynolds numbers. *Journal of Fluid Mechanics* 1985; **154**: 215–230.
7. Oliver DLR, Chung JN. Flow about a fluid sphere at low to moderate Reynolds numbers. *Journal of Fluid Mechanics* 1987; **177**: 18.

8. Nguyen HD, Paik S, Chung JN. A combined Galerkin/collocation spectral method for transient solution of flow past a spherical droplet. In *Two-Phase Flow in Energy Exchange Systems*, Sohal MS, Rabas TJ (eds). The American Society of Mechanical Engineers: New York, 1992; 87.
9. Oliver DLR, Chung JN. Conjugate unsteady heat transfer from a spherical droplet at low Reynolds numbers. *International Journal for Heat Mass Transfer* 1986; **29**: 879–887.
10. Oliver DLR, Chung SN. Unsteady conjugate heat transfer from a translating fluid sphere at moderate Reynolds numbers. *International Journal for Heat Mass Transfer* 1990; **33**: 401–408.
11. Nguyen HD, Paik S, Chung JN. Unsteady conjugate heat transfer associated with a translating spherical droplet: a direct numerical simulation. *Numerical Heat Transfer. Part A* 1993; **24**: 161–180.
12. Gottlieb D, Orszag SA. *Numerical Analysis of Spectral Methods: Theory and Applications*. SIAM: Philadelphia, PA, 1977.
13. Patera AT. A spectral element method for fluid dynamics: laminar flow in a channel expansion. *Journal of Computers in Physics* 1984; **54**: 468–488.
14. Lin CL, Lee SC. Transient state analysis of separated flow around a sphere. *Computers and Fluids* 1973; **1**: 235–250.
15. Chisnell RF. The unsteady motion of a drop moving vertically under gravity. *Journal of Fluid Mechanics* 1987; **176**: 443–464.
16. Canuto C, Hussaini MH, Quarteroni A, Zang TA. *Spectral Methods in Fluid Dynamics*. Springer: New York, 1988.
17. Fox L, Parker I. *Chebyshev Polynomials in Numerical Analysis*. Oxford University Press: London, 1968.
18. Rivkind VIa, Ryskin GM, Fishbein GA. Flow around a spherical drop at intermediate Reynolds numbers. *Applied Mathematics and Mechanics* 1976; **40**: 687.
19. Abdel-Alim AH, Hamielec AE. A theoretical and experimental investigation of the effect of internal circulation on the drag of spherical droplets falling at terminal velocity in liquid media. *Industrial Engineering and Chemical Fundamentals* 1975; **14**: 308–312.
20. Elzinga ER, Banchero JT. Some observations on the mechanics of drops in liquid–liquid systems. *American Institute of Chemical Engineers Journal* 1961; **7**: 394.
21. Clift R, Grace JR, Weber ME. *Bubbles, Drops, and Particles*. Academic Press: New York, 1978.
22. Froessling N. *Gerlands Beitr. Geophysics* 1938; **52**: 170.
23. Nguyen HD, Paik S, Chung JN. Unsteady mixed convection heat transfer from a solid sphere: the conjugate problem. *International Journal for Heat Mass Transfer* 1993; **36**: 4443–4453.

